https://doi.org/10.5194/egusphere-2026-3007
Preprint. Discussion started: 29 June 2026

Spatial resolution versus precision in CO_2 point-source emission retrievals from the DQ-1 spaceborne lidar

Ruijie Zhang[1,2], Lu Zhang[2,3], Xingying Zhang[2,*], Peng Zhang[4,*], Minqiang Zhou[5], Xifeng Cao[2,3], Chonghui Cheng[6], Huirong Yang[5]

[1]Chinese Academy of Meteorological Sciences, China Meteorological Administration, Beijing, 100081, China
[2]Key Laboratory of Radiometric Calibration and Validation for Environmental Satellites, National Satellite Meteorological Center (National Center for Space Weather), Innovation Center for FengYun Meteorological Satellite (FYSIC), China Meteorological Administration (CMA), Beijing, 100081, China
[3]Youth Innovation Team of China Meteorological Administration " Validation of Fengyun Satellite Remote Sensing Products", Beijing, 100081, China
[4]Meteorological Observation Center, China Meteorological Administration (CMA), Beijing, 100081, China
[5]Institute of Atmospheric Physics, Chinese Academy of Sciences, Beijing, 100029, China
[6]State Key Laboratory of Extreme Photonics and Instrumentation, College of Optical Science and Engineering, Zhejiang University, Hangzhou, 310027, China

Correspondence to: Xingying Zhang (zxy@cma.gov.cn), Peng Zhang(zhangp@cma.gov.cn)

Abstract. This study examines the trade-off between spatial resolution and measurement precision in satellite-based quantification of CO_2 point-source emissions using observations from DQ-1, the first spaceborne active CO_2 lidar mission. Allan deviation analysis is used to characterize scale-dependent random errors in XCO_2 retrievals over homogeneous surfaces, and the resulting error estimates are incorporated into Gaussian plume simulations to evaluate how spatial averaging affects emission retrieval under different emission strengths, wind speeds, and observation distances. The results show a nonlinear response: moderate averaging reduces random noise and improves retrieval stability, whereas excessive averaging degrades plume representation through loss of spatial resolution. The preferred averaging scale depends mainly on emission strength, transport distance, and local plume geometry. For strong idealized sources (2000 kg s^{-1}), 50–100 averaging points (3.5–7 km) generally provide the best compromise in favorable controlled simulations, with R^2 values up to 0.68. For weak sources (500 kg s^{-1}), single-overpass estimates remain close to the detection limit even after averaging ($R^2 <$ 0.10). Application to seven DQ-1 overpasses of power plants shows that retrieved emissions are often more consistent with reference inventories at intermediate-to-coarse averaging scales, especially 75–150 points (5.25–10.5 km), but this range should not be interpreted as a universal optimum. The agreement should instead be treated as an inventory-based consistency check rather than an independent validation of instantaneous emissions. These findings provide a quantitative basis for choosing spatial averaging scales in DQ-1 point-source applications and identify the main conditions under which single-overpass lidar retrievals are likely to be informative.

https://doi.org/10.5194/egusphere-2026-3007
Preprint. Discussion started: 29 June 2026

1 Introduction

Atmospheric carbon dioxide (CO_2) concentrations have continued to increase over recent decades and remain the dominant anthropogenic greenhouse gas driving positive radiative forcing and climate change (Piao et al., 2009; Arias et al., 2021). Since the Industrial Revolution, atmospheric CO_2 levels have risen by approximately 50%, reaching ~420 ppm, largely as a result of fossil fuel combustion and industrial activities (Friedlingstein et al., 2022). Global anthropogenic CO_2 emissions exceeded 40.7 Gt yr^{-1} in 2022, with the energy and industrial sectors contributing nearly 60% of the total, and coal-fired power plants accounting for more than 40% of point-source emissions (Andrew, 2020; Cusworth et al., 2021; Shi et al., 2023a; Yang et al., 2023). Accurate monitoring of CO_2 emissions from large point sources is therefore essential for emission verification and climate policy implementation, as emphasized by international frameworks such as the Paris Agreement (Qin et al., 2022).

Satellite-based remote sensing provides a unique capability for monitoring CO_2 point-source emissions in a transparent, independent, and globally consistent manner (Schwandner et al., 2017; Dennison et al., 2013). This capability is particularly important for regions lacking dense ground-based monitoring networks or routine emission verification systems (Shi et al., 2020; Erland et al., 2022). Substantial progress has been achieved using passive satellite observations. Early studies demonstrated the feasibility of quantifying power plant emissions using OCO-2 XCO_2 data (Nassar et al., 2017), followed by advances integrating Gaussian plume models and chemical transport models for emission inversion (Zheng et al., 2019, 2020; Chevallier et al., 2022). Multi-overpass analyses have further improved retrieval robustness and explanatory power (Nassar et al., 2021; Lin et al., 2023), while long-term datasets from OCO-2/3 have enabled emission characterization of multiple power plants worldwide (Guo et al., 2023).

Compared with passive sensors, active remote sensing lidar offers distinct advantages for point-source emission monitoring. The well-defined laser path and narrow spectral linewidth enable improved sensitivity to localized concentration enhancements, particularly for strong emission sources (Kiemle et al., 2017; Wang et al., 2022b). Airborne and ground-based lidar experiments have demonstrated promising results, achieving emission estimates consistent with inventories and in situ measurements (Amediek et al., 2017; Mao et al., 2021; Shi et al., 2023b). In April 2022, China launched its first spaceborne active CO_2 mission, AEMS/DQ-1, equipped with an Integrated Path Differential Absorption (IPDA) lidar capable of global XCO_2 observations with high precision and day–night coverage (Ke et al., 2022; Fan et al., 2024). Validation studies indicate that DQ-1 XCO_2 measurements achieve accuracies better than 1 ppm (Zhang et al., 2024), and initial applications using the EMI-GATE model have demonstrated its potential for power plant emission estimation (Han et al., 2024).

Despite these advances, satellite-based quantification of CO_2 point-source emissions remains fundamentally constrained by the trade-off between spatial resolution and measurement precision. Instrument design limitations imply that improvements in spatial resolution are often accompanied by reduced signal-to-noise ratio or spectral resolution, which directly affect the detectability of concentration enhancements (Kruse et al., 2001). High spatial resolution is critical for resolving narrow plume structures and isolating point-source signals, whereas high measurement precision is essential for suppressing random

https://doi.org/10.5194/egusphere-2026-3007
Preprint. Discussion started: 29 June 2026

noise and reliably detecting weak enhancements. Current area-flux-mapping missions (e.g., OCO-2, OCO-3, GOSAT, TROPOMI) achieve high precision but are limited by relatively coarse spatial resolution, leading to plume broadening and reduced sensitivity to individual point sources (Brunner et al., 2023). Conversely, emerging high-resolution imagers and spaceborne lidars improve plume delineation but remain affected by measurement uncertainty due to instrument trade-offs (Jiang et al., 2025). A quantitative understanding of how spatial resolution and random error jointly influence emission retrieval performance is therefore critical for optimizing observation strategies and improving emission estimates.

This study employs Allan deviation analysis to characterize the dependence of random errors in DQ-1 XCO_2 observations on spatial scale and to evaluate spatial averaging strategies that balance plume resolvability against measurement precision. We combine Gaussian plume simulations with emission-rate inversions from selected real overpass observations over power plants to examine how averaging scale affects retrieval performance. The analysis is intended to quantify retrieval sensitivity and practical applicability rather than to provide a complete operational emission product. The remainder of this paper is organized as follows. Section 2 describes the data sources and methodologies, including Allan deviation analysis, random error characterization over homogeneous surfaces, case selection, and the emission inversion approach. Section 3 presents the main results from idealized Gaussian plume simulations and emission estimates derived from real power plant case studies. Section 4 discusses the trade-off between spatial resolution and measurement precision, the limitations of the current assumptions, comparisons with previous studies, and directions for future work.

2 Data and methods

2.1 Data source and preprocessing

2.1.1 ACDL XCO_2 products

ACDL is the world's first spaceborne IPDA lidar, developed by the Shanghai Institute of Optics and Fine Mechanics, Chinese Academy of Sciences, and mounted on a satellite platform provided by China Aerospace Science and Technology Corporation (Fan et al., 2024). Its primary objective is to conduct high-precision measurements of global atmospheric carbon dioxide. The instrument employs a nadir observation mode with a beam divergence angle of 0.1 milliradians, an along-track footprint of approximately 70 meters, a system repetition frequency of 20 Hz, a receiving telescope aperture of 1000 mm, and uses avalanche photodiodes (APD) for signal detection (Wu et al., 2024).

ACDL comprises three spectral channels: 1572 nm for carbon dioxide detection, and 532 nm and 1064 nm for cloud and aerosol detection. The column-averaged dry-air mole fraction of CO_2 (XCO_2) is retrieved through the 1572 nm channel. In this spectral band, the instrument alternately emits two laser pulses at closely spaced wavelengths: the online wavelength at 1572.024 nm, located on a strong CO_2 absorption line, and the offline wavelength at 1572.085 nm, located in a region of minimal absorption. The pulse interval is 200 μs to ensure footprint overlap (Liu et al., 2024; Wang et al., 2020). The online signal is sensitive to CO_2 concentration, while the offline signal serves as a reference. Because the two wavelengths are very

https://doi.org/10.5194/egusphere-2026-3007
Preprint. Discussion started: 29 June 2026

close, differences in water-vapor absorption and aerosol scattering are largely cancelled, allowing retrieval of column-averaged CO_2 concentration through differential absorption (Abshire et al., 2013; Zhu et al., 2019). This study uses DQ-1/ACDL XCO_2 data from June to December 2024.

2.1.2 Emission inventory

A global power plant emission inventory was constructed by integrating multiple public datasets. The Carbon Brief global coal power plant database and the Climate TRACE emission inventory (Climate TRACE, 2023) were jointly used to identify high-emitting power plants and to provide annual or multi-temporal reference emission rates. Because globally consistent hourly generation and stack-level operational data are not available, these inventory values cannot be treated as exact instantaneous emissions at the satellite overpass time. In this study they are therefore used as external consistency references for case screening and comparison, with Climate TRACE serving as the primary reference inventory.

2.1.3 Wind field

Wind fields were obtained from the ECMWF ERA5 reanalysis, providing hourly U and V wind components at 0.25° spatial resolution (Hersbach et al., 2020). Wind vectors were interpolated to the plume transport height assuming a stack height of 250 m (Hu and Shi, 2021). Near-surface winds were taken from ERA5-Land hourly wind products.

2.2 Emission inversion and uncertainty sources

Gaussian plume models are widely used for monitoring point source emissions due to their stability (Brusca et al., 2016). This study applies this method to spaceborne IPDA lidar to estimate CO_2 emissions from power plants. The basic equation of the model is as follows (Bovensmann et al., 2010):

$$\Delta Q(x,y) = \frac{F}{\sqrt{2\pi}a \cdot u\left(\frac{x}{x_0}\right)^{0.894}} e^{-\frac{1}{2}\left(\frac{y}{a\cdot\left(\frac{x}{x_0}\right)^{0.894}}\right)^2} \quad (1)$$

Where x and y represent the distances from the chimney along the wind direction and vertical to the wind direction (m), ΔQ is the total CO_2 column increment (g m^{-2}), F is the point source CO_2 emission rate (g s-1), and a is the atmospheric stability parameter, which is related to the solar radiation index and surface wind speed. The solar radiation index can be assessed using high cloud cover, low cloud cover, and solar elevation angle (Pasquill, 1961; Beals, 1971). The total CO_2 column amount 130 converted to the increment of column concentration ΔXCO_2 (ppm) can be calculated using the following equation (Zheng et al., 2020):

$$\Delta XCO_2(x,y) = \Delta Q(x,y) \cdot \frac{M_{air}}{M_{CO_2}} \cdot \frac{g}{P_{surf} - w \cdot g} \cdot 1000 \quad (2)$$

https://doi.org/10.5194/egusphere-2026-3007
Preprint. Discussion started: 29 June 2026

Where M_{air} is the molecular mass of dry air (g mol^{-1}), M_{CO_2} is the molecular mass of carbon dioxide (g mol^{-1}), g is the acceleration due to gravity, P_{surf} is the surface pressure (Pa), and w is the water vapor column content (kg m^2). To isolate the contribution from power plant emissions, the XCO_2 enhancement must be extracted from the satellite-observed column-averaged dry-air mole fraction. The dispersion of carbon dioxide plumes can be represented using a two-dimensional Gaussian framework. Because the spaceborne lidar's ground footprint intersects the plume along a near-transverse line, the observed cross-section approximates a one-dimensional Gaussian shape. In this study, we assume that the background carbon dioxide concentration varies linearly with a small gradient, and thus the observed distribution can be expressed as a combination of a linear background term and a Gaussian enhancement term:

$$XCO_2(x) = XCO_2b + b \cdot x + \frac{a}{\sigma\sqrt{2\pi}} e^{[-(x-\mu)^2/2\sigma^2]} \quad (3)$$

Where $XCO_2b + b \cdot x$ is background value of XCO_2, $\frac{a}{\sigma\sqrt{2\pi}} e^{[-(x-\mu)^2/2\sigma^2]}$ is ΔXCO_2 caused by power plant emissions (Reuter et al., 2019).

For DQ-1 orbital data, we selected overpasses where the downwind direction of the point source was approximately aligned with the satellite ground track and the observed carbon dioxide enhancement occurred within 50 km of the source. In the simulation experiments, the x-axis of the Gaussian plume corresponds to the direction of plume transport. Although many previous studies use wind vectors extracted from ERA5 reanalysis at plume height (Guo et al., 2023), instantaneous wind directions from reanalysis products may not always represent the actual plume transport direction at the time and scale of an overpass. We therefore used the vector from the stack to the fitted Gaussian peak as an observation-based plume-direction constraint and retained only cases where the angle between this direction and the interpolated wind was less than 25 degrees. This filtering reduces obvious wind-geometry mismatches but does not eliminate uncertainty in wind speed, boundary-layer structure, or plume rise. For the selected observations, we applied least-squares fitting to the Gaussian plume model to estimate the plant carbon dioxide emission rate, following Eqs. (2) and (3). Atmospheric stability, which strongly influences plume dispersion, was determined using the Pasquill-Gifford method based on cloud cover and solar elevation angle.

2.3 Principle of Allan deviation

Allan deviation is used to quantify the dependence of random error on averaging scale in along-track XCO_2 observations. Continuous satellite measurements are treated as discrete sequences, with footprint spacing defining the sampling interval. By applying grouped averaging with increasing averaging factors, Allan deviations are calculated to characterize scale-dependent noise behavior.

$$\sigma^2_{XCO_2}(\tau) = \frac{1}{2(M-1)} \sum_{k=1}^{M-1} \left[\overline{XCO_2}_{k+1}(\tau) - \overline{XCO_2}_{k}(\tau)\right]^2 \quad (4)$$

In systems dominated by white noise, the Allan deviation follows a $\tau^{-1/2}$ relationship, indicating that random errors can be reduced through averaging. Here τ represents the length of the time interval over which statistical averaging is performed.

https://doi.org/10.5194/egusphere-2026-3007
Preprint. Discussion started: 29 June 2026

Because the ACDL observations are sampled at uniform time intervals, τ can be represented by the corresponding number of observations. The Allan deviation curves derived from homogeneous surface areas therefore provide a quantitative relationship between random error magnitude and spatial resolution, represented by the number of averaged points or the equivalent averaging time. This relationship provides the basis for evaluating spatial averaging strategies for XCO_2 emission retrieval.

To investigate the characteristics of random errors in ACDL CO_2 measurements under different surface scenarios, Allan deviation analysis was performed using ACDL overpass observations over homogeneous surface regions, including desert and forested vegetation areas. The study regions are shown in Fig. 1: the desert region (Fig. 1a) corresponds to the Arabian Peninsula (35°E–60°E, 10°N–30°N), and the forested vegetation region (Fig. 1b) corresponds to the high-latitude taiga belt (40°E–140°E, 50°N–70°N). These regions were selected as representative homogeneous surfaces because they exhibit relatively uniform surface reflectance and limited seasonal variability, helping ensure that observed XCO_2 variations are dominated mainly by instrument random error rather than surface-induced or anthropogenic signals. Both regions also have frequent clear-sky conditions and low cloud contamination. The longest continuous segments (>1500 points) were selected for Allan deviation evaluation. Observations were further filtered to include only land scenes under clear-sky conditions with a signal-to-noise ratio (SNR) greater than 50. From July to December 2024, DQ-1 ACDL acquired 18 overpass scenes over the desert region and 6 overpass scenes over the forested vegetation region. Allan deviation was calculated for different averaging points using the AVS (averaging of signals) method (Tellier et al., 2018), which first averages the online and offline calibrated signals separately before computing differential absorption optical depth and XCO_2. This reduces statistical bias induced by the nonlinearity of the lidar equation by increasing the effective SNR of the averaged signals. Fig. 2 compares the Allan deviation of XCO_2 over the two homogeneous surface types as a function of averaging points. For both regions, Allan deviation decreases with increasing averaging points. Over the desert region, Allan deviation is approximately 7.41–9.92 ppm at small averaging lengths (5 points), with a mean value of 8.76 ppm. When the averaging points increase to 20, Allan deviation decreases to approximately 3.25–5.55 ppm, with a mean value of 4.17 ppm. For averaging points greater than 100, the mean Allan deviation further decreases to approximately 1.90 ppm and reaches about 1.06 ppm at 150 points. In contrast, the forested vegetation region exhibits a similar overall decreasing trend but larger inter-orbit variability. At small averaging lengths (10–20 points), Allan deviation ranges from approximately 3.55 to 9.86 ppm. At intermediate averaging lengths (30–80 points), it mainly spans 1.52–4.19 ppm. When averaging points exceed 100, Allan deviations over both surface types gradually converge to comparable levels of approximately 1 ppm.

The Allan deviation derived at different averaging points provides a quantitative estimate of the random error associated with the corresponding spatial averaging scale. The obtained Allan deviation values are subsequently adopted as scale-dependent random error inputs in the simulation experiments to represent observation errors under different spatial averaging conditions.

https://doi.org/10.5194/egusphere-2026-3007
Preprint. Discussion started: 29 June 2026

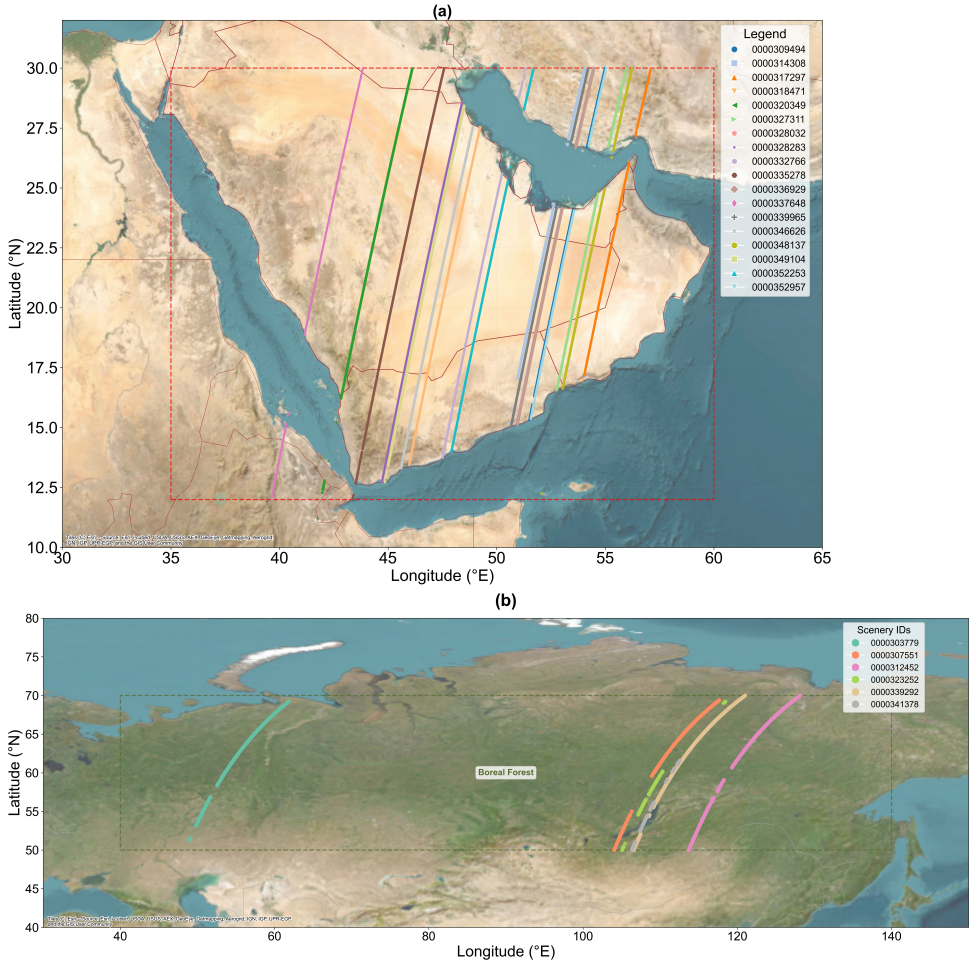

Figure 1. Study regions for Allan deviation analysis over homogeneous desert (a) and forested vegetation (b) surfaces. The base map was designed and developed by Esri | Powered by Esri.

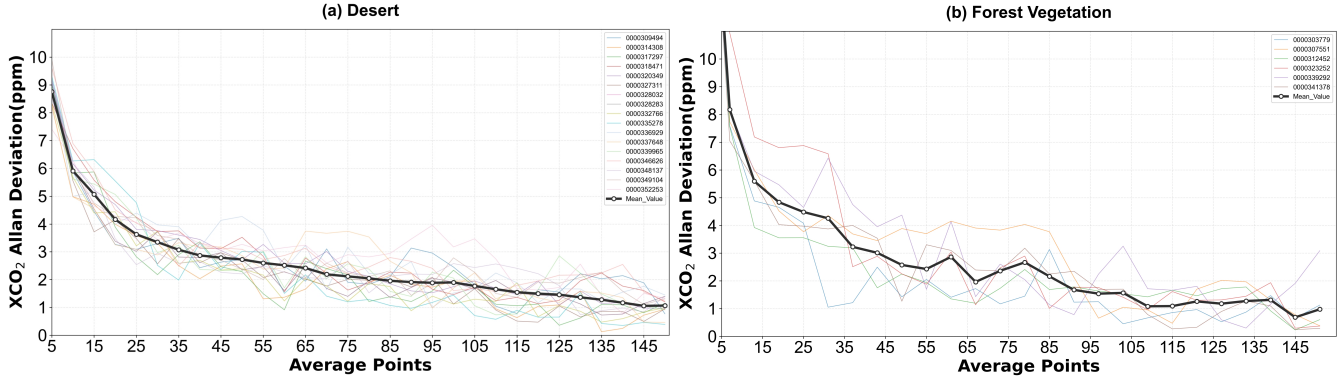

Figure 2. Allan deviation of XCO_2 as a function of averaging points over homogeneous desert (a) and forested vegetation (b) regions.

https://doi.org/10.5194/egusphere-2026-3007
Preprint. Discussion started: 29 June 2026

3 Results

3.1 Results from emission simulations

This section examines how spatial averaging affects plume representation and emission retrieval under controlled idealized conditions, and how this effect is modulated by emission strength, observation distance, and wind speed. Based on Allan deviation analysis (Section 2.3), scale-dependent random errors were introduced into simulated XCO_2 fields. Averaging points were set to 5, 15, 25, 50, 75, 100, 125, and 150, with random errors assigned according to the Allan deviation curve. Emission rates were set to 500, 1000, 1500, and 2000 kg s^{-1}; wind speeds to 2, 4, 6, 8, and 10 m s^{-1}; and observation distances to 2.5, 5, 7.5, and 10 km. Concentration fields were generated using the Gaussian plume model, so the simulations isolate the impact of random measurement error and spatial averaging and do not include all sources of atmospheric transport uncertainty. For each configuration, spatial resolution was defined as 70 m multiplied by the number of averaging points. Emission rates were then retrieved from simulated datasets with varying noise levels to assess the impact of averaging.

Fig. 3 illustrates how spatial averaging alters plume structure for an emission rate of 2000 kg s^{-1} and wind speed of 2 m s^{-1} (stability class B). As averaging increases, each pixel incorporates more background grid cells, progressively smoothing the plume. Turbulent diffusion patterns become blurred, reducing the ability to resolve full plume morphology. This effect is evident in pixel-level XCO_2 responses, which show pronounced nonlinear dependence on averaging scale. At the source (x = 0, y = 0; Fig. 4a), increasing averaging from 5 to 15 points reduces peak XCO_2 by 148.15 ppm, with an additional 182.64 ppm drop at 25 points. At 50 points, the plume is represented by only about five grid cells, and its structure is no longer fully resolved. Further increases to 75 and 100 points leave only two to three identifiable high-XCO_2 pixels. Similar behavior is observed at a downwind distance of 5 km (Fig. 4b), corresponding to a typical DQ-1 overpass. As averaging increases from 5 to 15 points, peak XCO_2 decreases from 21.89 to 20.23 ppm, and further to 20.07 ppm at 25 points. However, at 50 points, the enlarged pixel size coincides with the grid cell containing the maximum concentration near the source, causing peak XCO_2 to increase to 29.04 ppm. Beyond 75 points, plume broadening dominates, and peak values decrease again. These results demonstrate that plume representation responds non-monotonically to spatial averaging due to the combined effects of signal mixing and plume geometry.

https://doi.org/10.5194/egusphere-2026-3007
Preprint. Discussion started: 29 June 2026

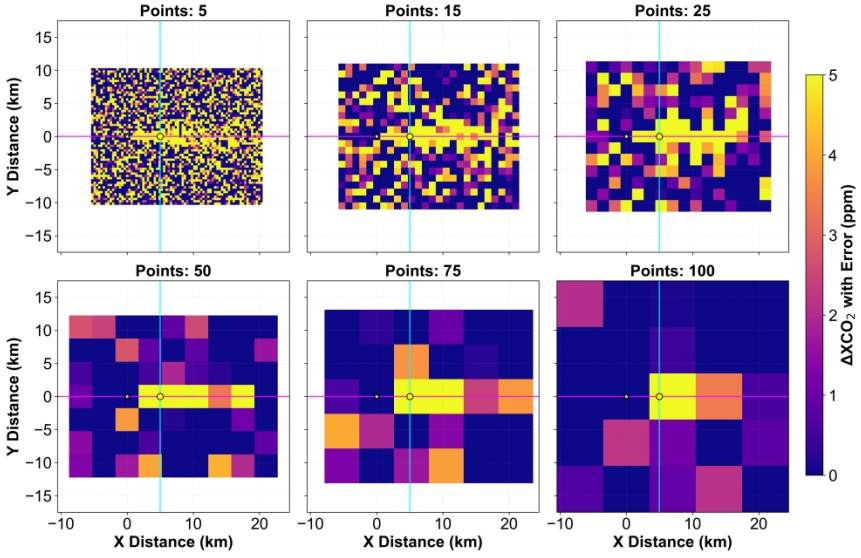

Figure 3. Simulated XCO_2 plume structures under different spatial averaging scales (2000 kg s^{-1}, 2 m s^{-1}).

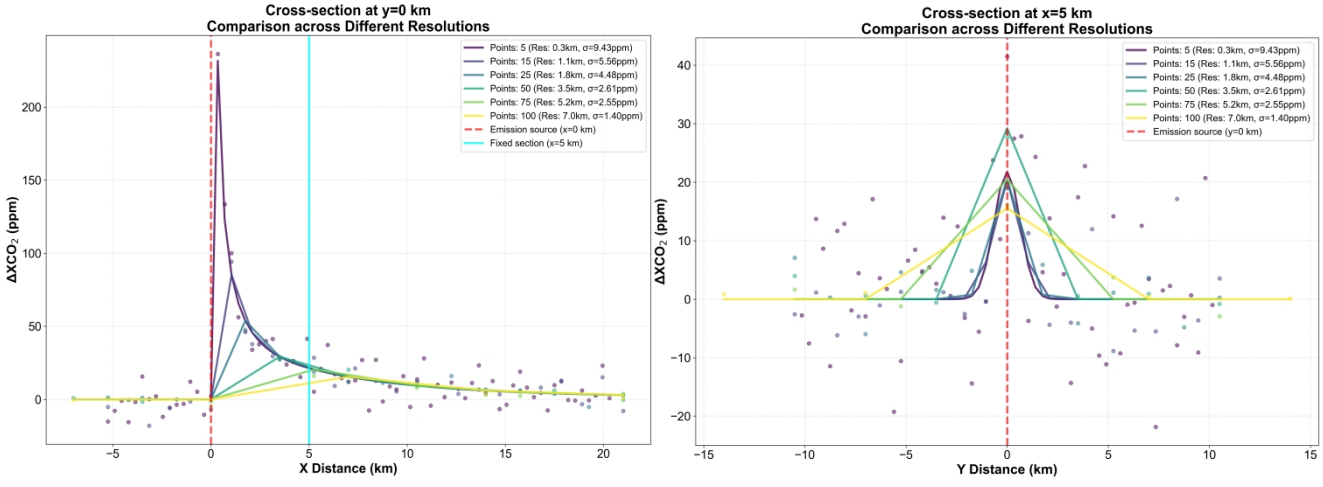

Figure 4. Pixel-level XCO_2 response to spatial averaging at y = 0 km (a) and x = 5 km (b).

Fig. 5 and Fig. 6 show the sensitivity of emission retrievals to averaging scale under different emission strengths (500, 1000, 2000 kg s^{-1}), with wind speed fixed at 2 m s^{-1} and distance at 7.5 km. For all scenarios, retrieved emission rates exhibit a pronounced nonlinear dependence on averaging points: performance improves rapidly, reaches a maximum, then declines slowly. This pattern mirrors the Allan deviation curve, reflecting the competing effects of noise suppression and resolution loss. For the low-emission case (500 kg s^{-1}), retrieval is highly sensitive to averaging. At 5 points, the retrieved rate is 554.92 kg s^{-1} (relative error 10.98%), but R^2 is negative (−0.03), indicating noise dominance. At 15–25 points, retrieved values drop to 449.51–444.79 kg s^{-1} (relative error −10% to −11%), but R^2 remains near zero. At 50–75 points, retrievals recover to 450.89–465.81 kg s^{-1} (relative error −6.84% to −9.82%), and R^2 becomes positive (0.10), suggesting effective noise

https://doi.org/10.5194/egusphere-2026-3007
Preprint. Discussion started: 29 June 2026

suppression. At 100–150 points, retrievals stabilize at 457.13–460.34 kg s^{-1} (relative error −7.93% to −8.57%), but R^2 declines slightly, indicating diminishing returns as resolution loss offsets noise reduction. For the moderate case (1000 kg s^{-1}), dependence on averaging is less pronounced but still evident. At 5 points, retrieved rate is 1002.95 kg s^{-1} (relative error 0.29%), but low R^2 (0.02) indicates poor reliability. At 15 points, retrieved rate drops sharply to 902.39 kg s^{-1} (relative error −9.76%). As averaging increases to 25, 50, and 75 points, retrievals recover to 917.74, 940.84, and 965.41 kg s^{-1}, with relative errors improving from −8.23% to −3.46% and R^2 climbing from 0.08 to 0.34. Beyond 75 points, retrievals stabilize at 954.65–958.97 kg s^{-1} (relative error −4.10% to −4.53%), with slight R^2 decline. For the high-emission case (2000 kg s^{-1}), retrieval improves rapidly with averaging and plateaus. At 5 points, retrieved rate is 1977.09 kg s^{-1} (relative error −1.15%), but low R^2 (0.15) indicates variability. At 15–50 points, retrievals rise from 1889.40 to 1940.82 kg s^{-1}, with relative errors shrinking from −5.53% to −2.96% and R^2 increasing from 0.20 to 0.41. At 75 points, performance peaks at 1965.39 kg s^{-1} (relative error −1.73%, R^2 = 0.68), representing the best balance in this configuration between noise suppression and resolution preservation. Beyond 75 points, retrievals stabilize at 1954.62–1958.95 kg s^{-1} (relative error −2.05% to −2.27%, R^2 = 0.56–0.60), indicating diminishing returns. The R^2 heatmap (Fig. 6) shows that higher R^2 regions align with reduced relative error, forming curved contours that highlight the nonlinear trade-off between averaging and accuracy. At large scales (≥75 points), further averaging yields only marginal error reductions (<2–3 percentage points), while R^2 approaches saturation.

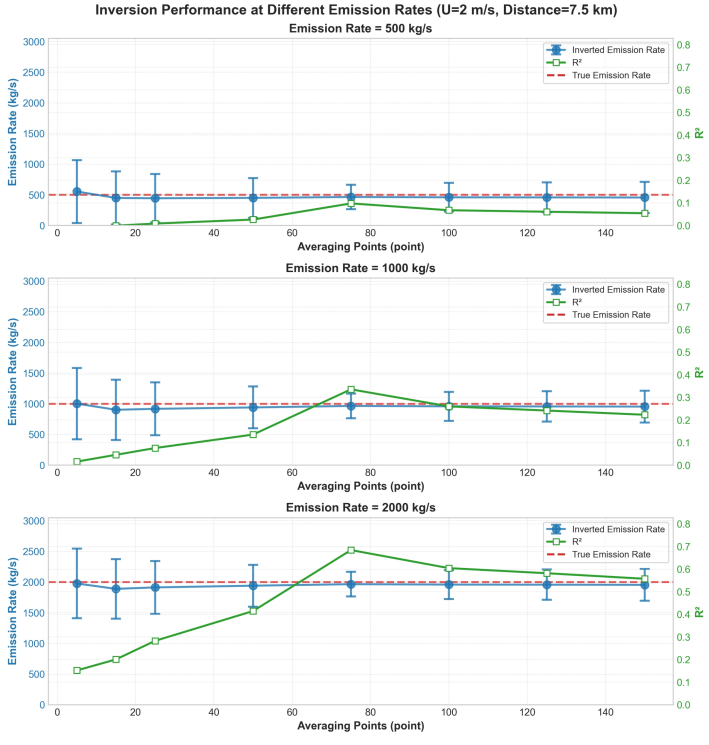

Figure 5. Dependence of retrieved emission rates on spatial averaging scale for different emission strengths (500, 1000, and 2000 kg s^{-1}) at a fixed wind speed of 2 m s^{-1} and an observation distance of 7.5 km.

https://doi.org/10.5194/egusphere-2026-3007
Preprint. Discussion started: 29 June 2026

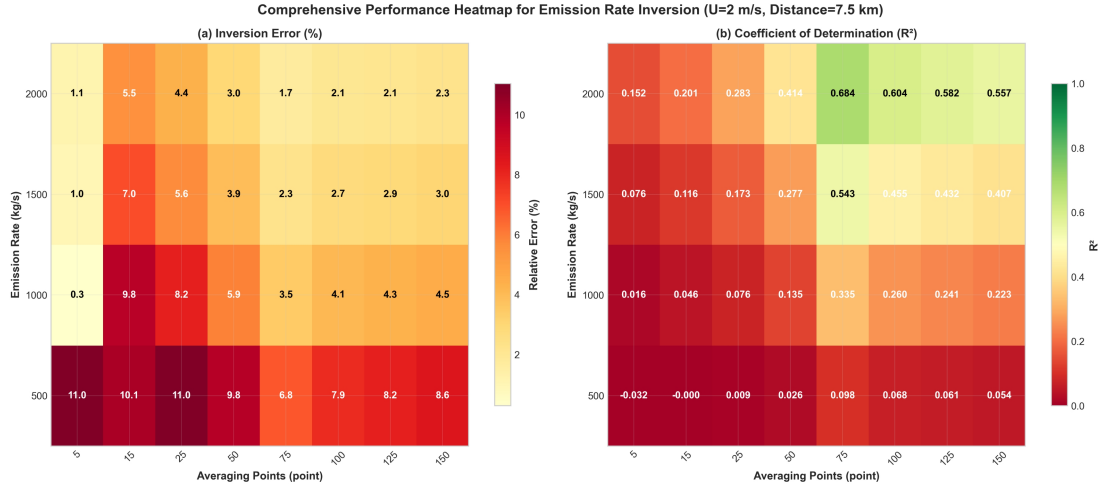

Figure 6. Inversion error (a) and R^2 (b) of emission-rate retrievals as functions of emission rate and spatial averaging points under a fixed wind speed of 2 m s^{-1} and an observation distance of 7.5 km.

To evaluate inversion performance under different emission intensities, we selected an averaging scale of 75 points (5.25 km resolution) and conducted simulations for 500, 1000, and 2000 kg s^{-1}. Fig. 7 shows XCO_2 plume distributions, and Fig. 8 presents concentration profiles at x = 7.5 km with least-squares fits. Plume extent and gradient increase with emission rate. At 500 kg s^{-1}, maximum concentration is approximately 5 ppm, with an along-wind extent of approximately 12 km. At 1000 kg s^{-1}, the maximum increases to approximately 10 ppm and the extent to 18 km. At 2000 kg s^{-1}, the maximum reaches approximately 18 ppm, with a similar extent. The fitting results show that the retrieval becomes more constrained as emission strength increases. At 500 kg s^{-1}, the weak signal yields a retrieved rate of 652.7 kg s^{-1} (relative bias 30.5%, R^2 = 0.178), indicating that the estimate is close to the detection limit under single-overpass conditions. At 1000 kg s^{-1}, the stronger signal yields 969.6 kg s^{-1} (bias -3.0%, R^2 = 0.403). At 2000 kg s^{-1}, the signal reaches 18.2 ppm and yields 1853.4 kg s^{-1} (bias -7.3%, R^2 = 0.698). These results indicate that the Gaussian plume fit is most informative for stronger sources, while weak-source estimates require additional constraints or multi-overpass aggregation.

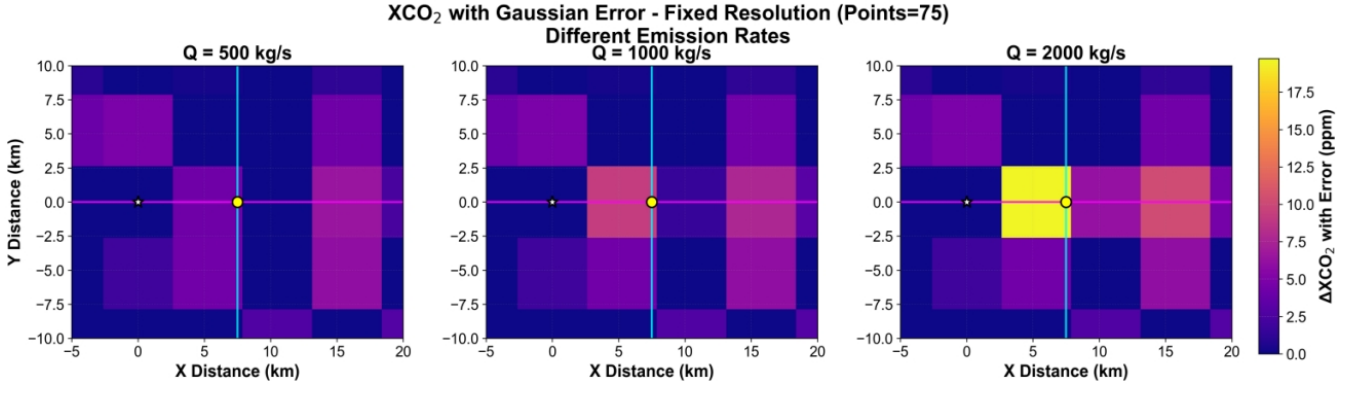

Figure 7. Simulated XCO_2 plume structures under different emission rates (500, 1000, and 2000 kg s^{-1}; 75 points; 2 m s^{-1}).

https://doi.org/10.5194/egusphere-2026-3007
Preprint. Discussion started: 29 June 2026

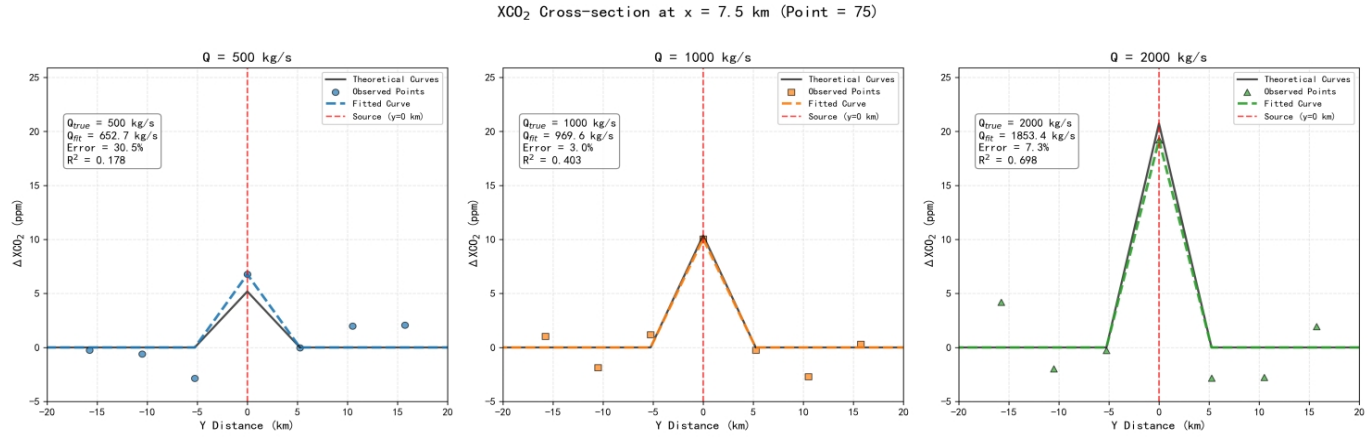

Figure 8. Concentration profiles at x = 7.5 km and least-squares fitting results for Q = 500 kg s^{-1} (a), Q = 1000 kg s^{-1} (b), and Q = 2000 kg s^{-1} (c).

Fig. 9 and Fig. 10 illustrate the dependence of inversion performance on observation distance (2.5, 5.0, 7.5, 10.0 km) at fixed emission rate (2000 kg s^{-1}) and wind speed (2 m s^{-1}). Distance critically controls accuracy, with larger averaging scales needed as distance increases. At 2.5 km, performance improves rapidly with averaging. At 15 points, retrieved rate is 1962.86 ± 213.76 kg s^{-1} (relative error 8.80%, R^2 = 0.65); at 25 points, it improves to 1977.44 ± 130.20 kg s^{-1} (error 5.36%, R^2 = 0.84). At ≥75 points, inversion fails (R^2 negative), indicating loss of statistical meaning. At 5.0 km, inversion shows greater sensitivity to averaging. At 25 points, retrieved rate is 1938.85 ± 340.80 kg s^{-1} (error 14.12%, R^2 = 0.41); at 50–75 points, performance improves to 1968.63 ± 181.17 kg s^{-1} (error 7.45%, R^2 = 0.73). Inversion failure recurs at 150 points. At 7.5 km, the most favorable performance occurs at 75 points: 1965.39 ± 199.90 kg s^{-1} (error 8.22%, R^2 = 0.68). At 50 points, retrieved rate is 1940.82 ± 341.03 kg s^{-1} (error 14.02%, R^2 = 0.41); at 100 points, it decreases slightly to 1958.95 ± 236.55 kg s^{-1} (error 9.72%, R^2 = 0.60). No inversion failure occurs across the full averaging range. At 10.0 km, performance deteriorates markedly. At 50 points, retrieved rate is 1892.17 ± 538.56 kg s^{-1} (error 22.64%, R^2 = 0.19); at 75 points, it is 1923.19 ± 430.69 kg s^{-1} (error 17.73%, R^2 = 0.30). Increasing to 100–150 points improves retrievals to 1954.62–1958.95 kg s^{-1} (error 9.72–10.65%), but R^2 remains below 0.60, and systematic underestimation persists. Increasing distance consistently degrades accuracy, and the error-reduction efficiency of additional averaging diminishes with distance (Fig. 10). At 7.5 km and beyond, performance saturates, and even extensive averaging cannot fully compensate for weakened observational constraints. Inversion failure occurs only at close range (≤5.0 km) with excessive averaging, reflecting practical limitations.

https://doi.org/10.5194/egusphere-2026-3007
Preprint. Discussion started: 29 June 2026

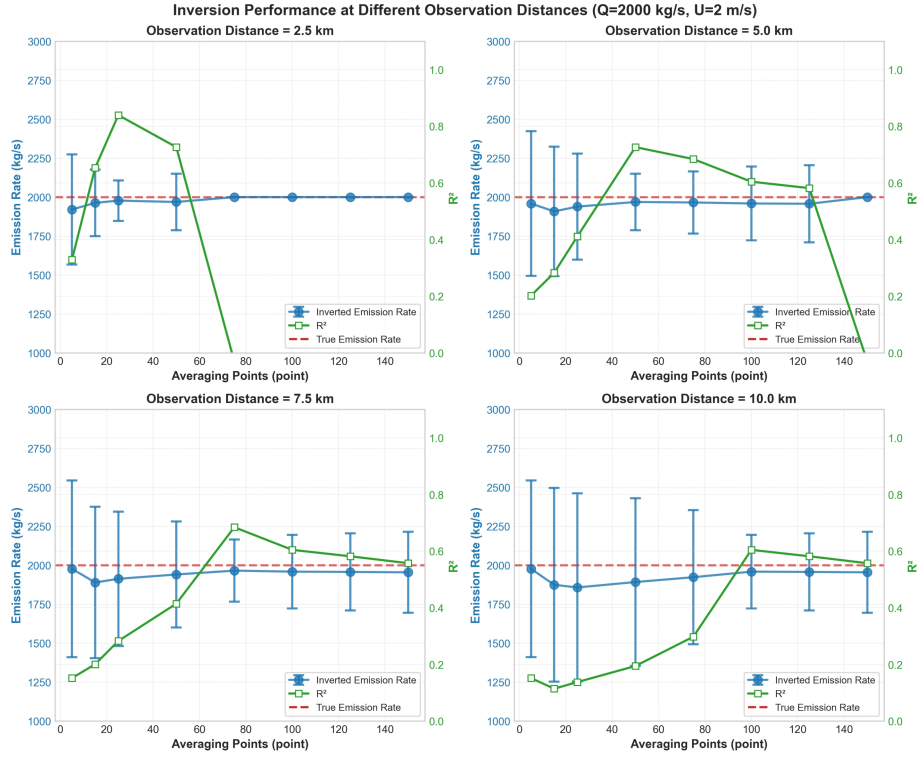

Figure 9. Retrieved emission rates as a function of spatial averaging points at different observation distances under an emission rate of 2000 kg s⁻¹ and a wind speed of 2 m s⁻¹.

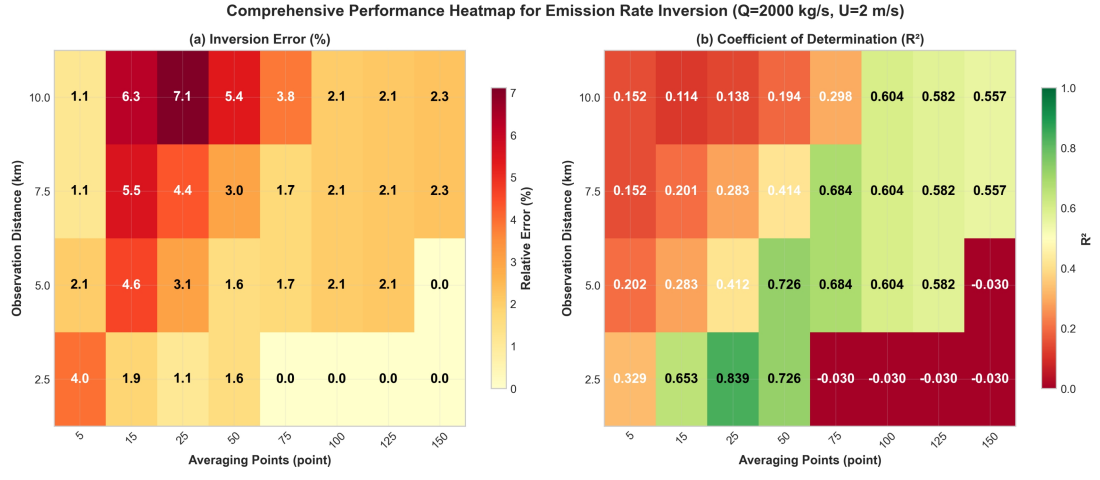

Figure 10. Inversion error (a) and R² (b) of emission-rate retrievals as functions of observation distance and spatial averaging points under a fixed wind speed of 2 m s⁻¹ and an emission rate of 2000 kg s⁻¹.

Fig. 11 and Fig. 12 show how wind speed (2, 4, 6, and 8 m s⁻¹) modulates the influence of averaging at fixed emission rate (2000 kg s⁻¹) and distance (7.5 km). Under clear-sky midday conditions, these wind speeds correspond to moderately

https://doi.org/10.5194/egusphere-2026-3007
Preprint. Discussion started: 29 June 2026

unstable to neutral stability. At 2 m s^{-1}, retrieval improves substantially with averaging, with the most favorable result at 75 points (1965.39 ± 199.90 kg s^{-1}; error 8.22%; R^2 = 0.68). At 4 m s^{-1}, the best case remains near 75 points, but the error increases to 16.43% and R^2 decreases to 0.34. At 6 m s^{-1}, the 75-point case gives an error of 11.17% and R^2 = 0.53. At 8 m s^{-1}, retrieval stability does not improve further, with an error of 14.90% and R^2 = 0.38 at 75 points. These results indicate that moderate averaging can improve retrievals under favorable wind conditions, but the error can still exceed 10–20% when plume dilution, transport distance, or stability conditions are less favorable. Therefore, the 50–100 point range should be interpreted as a useful scale window for the tested idealized cases, not as a guarantee of uniformly low retrieval error.

These results show that emission strength is the primary factor controlling retrieval reliability. For strong sources (2000 kg s^{-1}), the simulations indicate relatively stable performance under moderate wind speeds with 50–100 averaging points, although the exact relative bias depends on observation distance and wind configuration. For weak sources (500 kg s^{-1}), even optimized averaging yields weak explanatory power (R^2 < 0.10 in the scale-sensitivity experiment), suggesting that prior constraints, multi-overpass averaging, or alternative retrieval approaches are needed.

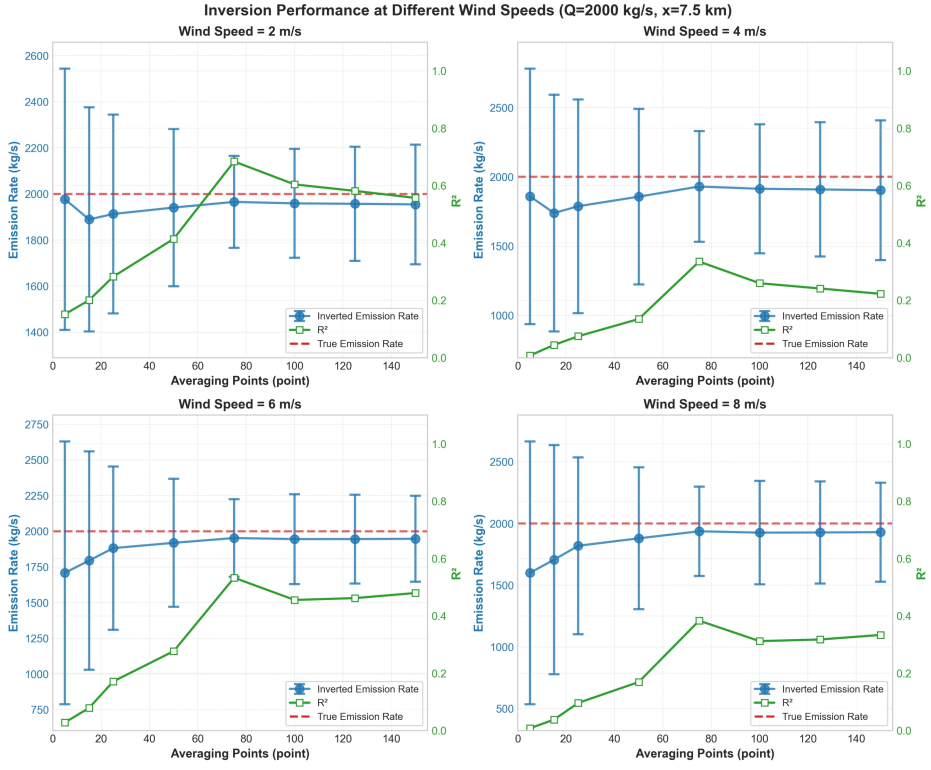

Figure 11. Retrieved emission rates as a function of spatial averaging points under different wind speeds (2, 4, 6, and 8 m s^{-1}) for a fixed emission rate of 2000 kg s^{-1} and an observation distance of 7.5 km.

https://doi.org/10.5194/egusphere-2026-3007
Preprint. Discussion started: 29 June 2026

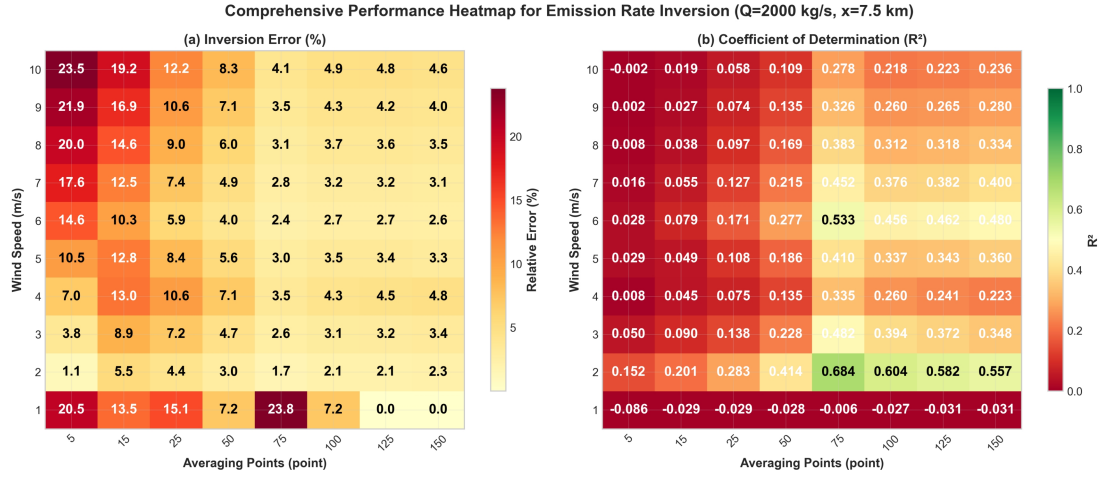

Figure 12. Inversion error (a) and R^2 (b) of emission-rate retrievals as functions of wind speed and spatial averaging points under a fixed emission rate of 2000 kg s^{-1} and an observation distance of 7.5 km.

3.2 Emission-rate retrieval results from ACDL observations

To examine the practical applicability of the results obtained in Section 3.1, this section applies the DQ-1 ACDL retrieval framework to real overpasses of point-source regions. Emission rates are estimated under different numbers of averaging points, with the aim of identifying averaging configurations that are most consistent with the observed plume structure and reference inventories.

The Majuba Power Station (approximately 4110 MW; Fig. 13a and Table 1), located in the South African Highland, was selected as a representative DQ-1 ACDL emission retrieval case. Situated at an elevation of 1700 m, the site has a relatively thin atmospheric column and low aerosol loading, which can enhance the lidar signal-to-noise ratio (SNR). On 1 June 2024 at 13:41 local time, we analyzed the spatial distribution of XCO_2 from a downwind overpass. This midday overpass was likely influenced by a developed convective boundary layer. Strong solar heating at this high-altitude station can promote vertical mixing and a deeper boundary layer, while solar background also contributes to measurement noise. At finer averaging scales (e.g., 5 points), XCO_2 exhibited pronounced spatial variability and localized plume-like spikes. As the averaging scale increased to 15-50 points, the range narrowed, reflecting suppression of random noise together with moderate smoothing. At larger scales (75-150 points), the distribution became more continuous. To evaluate consistency, estimated rates were compared with inventories from Climate TRACE (691.83 kg s^{-1}) and Carbon Brief (644.97 kg s^{-1}). At smaller scales ($N < 100$), emissions exceeded inventory values, probably because high-frequency stochastic variability inflated the fitted Gaussian amplitude. As N increased to 125, the retrieved value (806.70 ± 116.48 kg s^{-1}) approached the inventory range, although remaining higher than both references. This result suggests a preferred scale between 125 and 150 points for the daytime Majuba case, while also highlighting the need to interpret inventory agreement cautiously because the inventories do not represent instantaneous stack emissions.

https://doi.org/10.5194/egusphere-2026-3007
Preprint. Discussion started: 29 June 2026

To evaluate performance in a polluted nighttime environment, the retrieved emission rates for the Lalitpur station (Fig. 13b and Table 1) in India were analyzed from an overpass on 21 October 2024 at 01:52 local time. Unlike the daytime Majuba case, the Lalitpur overpass sampled the atmosphere during a stable nocturnal boundary layer. In the Indo-Gangetic Plain, nighttime stability can trap industrial emissions and aerosols near the surface. Although the absence of solar background can improve raw SNR, horizontal heterogeneity in stratified nocturnal layers may introduce substantial background structure. The results show a more complex sensitivity to N. At small scales (N = 5-25), emissions show a large positive bias (1959.78-7522.68 kg s^{-1}), consistent with unstable fitting caused by unresolved background variability and plume-like local enhancements. At N = 75, the retrieved rate (447.97 ± 103.04 kg s^{-1}) is close to the reference inventory value of 451.49 kg s^{-1}. As N increases to 100-125, estimates rebound, likely reflecting background inhomogeneity from surrounding nocturnal agricultural or industrial activity, and at N = 150 the plume signal is over-smoothed. The comparison between the daytime Majuba and nighttime Lalitpur cases indicates that the optimal averaging scale is influenced by transport distance, boundary-layer regime, surface reflectance, and background heterogeneity. DQ-1 ACDL can provide useful constraints under both daytime and nighttime conditions, but polluted nighttime regions require a narrower and more carefully screened averaging-scale search.

To evaluate the practical applicability of the spatial averaging strategy derived from simulations, we performed emission-rate retrievals for seven representative CO_2 point sources worldwide using real DQ-1 ACDL XCO_2 products (Table 2). These cases cover different surface reflectivities, including sandy terrain in South Africa and forested regions of Russia, as well as both diurnal and nocturnal conditions and a range of emission intensities. The observational results in Table 3 show a nonlinear response of retrieval behavior to the number of averaging points, consistent with the theoretical trade-off between SNR and spatial resolution. For example, in the Surgut GRES-1 and 2 case in Russia, a high-emission source reported at 987.53 kg s^{-1}, an averaging scale of 150 points (approximately 10.5 km) yielded a retrieved emission rate of 1022.17 ± 144.46 kg s^{-1}. The small difference relative to the inventory suggests that extensive averaging can suppress random instrument noise for strong plumes without completely removing the main concentration gradient. Similarly, the Majuba power plant in South Africa, located over a high-albedo sandy surface, benefited from relatively favorable lidar backscatter; under an averaging scale of 125 points, retrievals from two separate overpasses (806.70 and 850.97 kg s^{-1}) showed good internal consistency. The cases also indicate that the preferred averaging scale is modulated by local wind fields and observation geometry. In the Wucaiwan (China) case, characterized by low surface wind speed (1.94 m s^{-1}) and short observation distance (12.3 km), excessive averaging tended to dilute sharp concentration peaks. Applying a more moderate scale of 110 points yielded 583.67 ± 73.17 kg s^{-1}, within 10% of the Carbon Brief inventory. The nocturnal Reftinskaya GRES case demonstrates a useful capability of active sensing under no-sunlight conditions; despite forest cover and a more complex nighttime boundary layer, the model produced a plausible estimate (884.07 ± 65.47 kg s^{-1}) at 150 averaging points. These comparisons support the existence of a scale-dependent trade-off in real overpasses, but they do not prove that 75–150 points is a universal optimum. Rather, this range produced relatively good inventory consistency for several selected cases. Several sources of uncertainty remain. Allan-deviation-based averaging suppresses random errors, but systematic biases may

https://doi.org/10.5194/egusphere-2026-3007
Preprint. Discussion started: 29 June 2026

arise from ERA5 wind resolution, plume-height assumptions, atmospheric stability parameterization, background fitting, plume rise, and the temporal mismatch between satellite overpasses and inventory reference periods. Preliminary sensitivity tests indicate that a 1 m s^{-1} bias in wind speed typically results in an emission retrieval uncertainty of approximately 10–15%, consistent with previous satellite-based point-source studies (Nassar et al., 2017; Reuter et al., 2019). A complete uncertainty budget is still required before operational use for emission verification.

Table 1. Gaussian fitting parameters and emission estimates derived from the cross-sectional flux method under different spatial averaging scales for the Majuba and Lalitpur power plants.

Averaging number (N)	Majuba Baseline (ppm)	Majuba R^2	Majuba Q ± σ (kg s^{-1})	Lalitpur Baseline (ppm)	Lalitpur R^2	Lalitpur Q ± σ (kg s^{-1})
5	418.55 ± 2.15	0.93	4931.33 ± 2246.15	423.04 ± 4.56	0.13	1959.78 ± 1503.49
15	420.73 ± 1.08	0.87	4469.47 ± 1829.51	425.82 ± 2.72	0.61	5626.96 ± 182.76
25	417.31 ± 2.03	0.86	3620.81 ± 1674.56	429.78 ± 2.27	0.75	7522.68 ± 123.13
50	415.09 ± 0.76	0.79	3567.88 ± 1464.59	—	—	—
75	414.23 ± 0.53	0.87	2713.95 ± 1129.26	446.41 ± 0.24	0.85	**447.97 ± 103.04**
100	414.89 ± 0.20	0.91	1395.65 ± 356.57	446.28 ± 0.21	0.77	1120.84 ± 111.44
125	414.75 ± 0.19	0.71	**806.70 ± 116.48**	445.18 ± 0.20	0.84	1690.12 ± 150.66
150	414.73 ± 0.12	0.74	365.82 ± 95.68	441.53 ± 0.08	0.95	217.36 ± 73.48
Inventory	—	—	**645.0(Carbon Brief)/691.8(Climate TRACE)**	—	—	**451.5(Carbon Brief)**

https://doi.org/10.5194/egusphere-2026-3007
Preprint. Discussion started: 29 June 2026

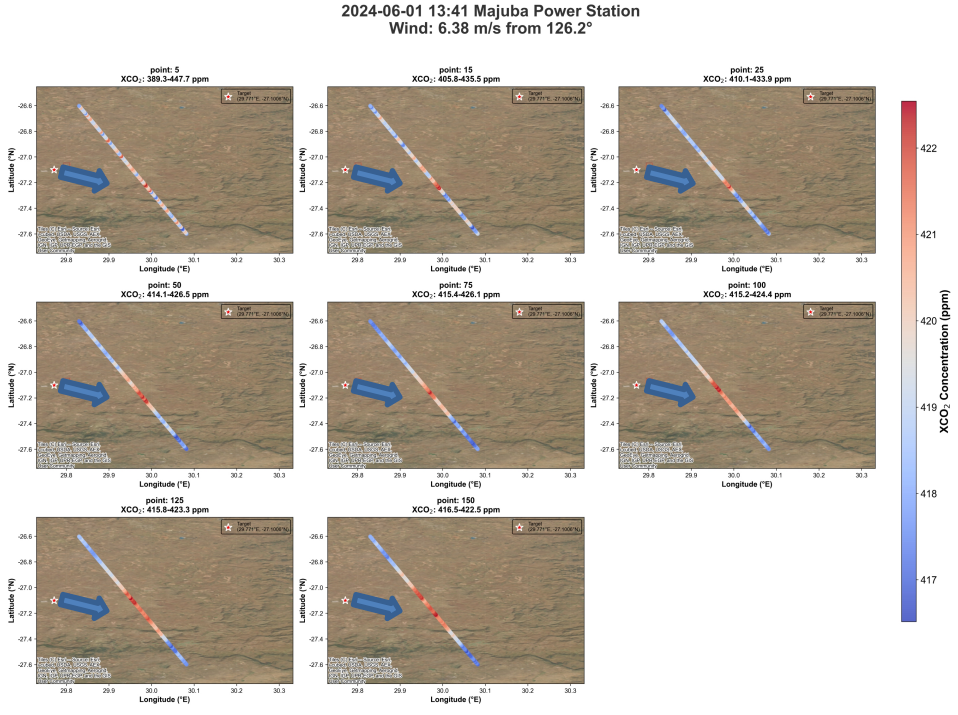

370

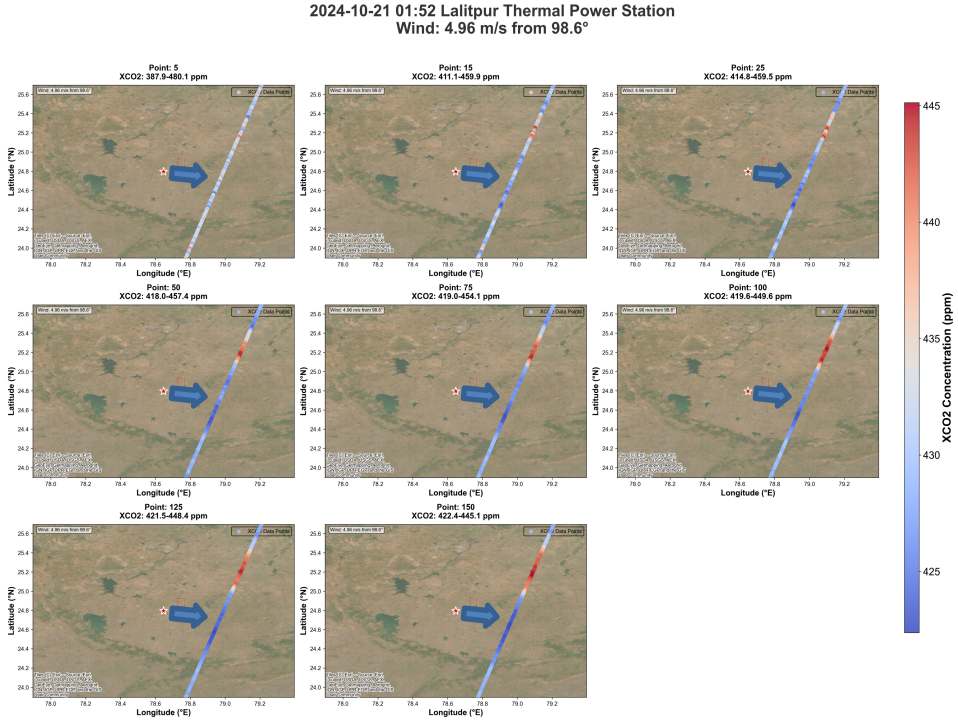

Figure 13. Multi-scale averaging of XCO_2 along the DQ-1 ACDL overpass track over the Majuba Power Station (2024-06-01 13:41) and Lalitpur Thermal Power Station (2024-10-21 01:52). Panels correspond to averaging units comprising 5, 15, 25, 50, 75, 100, 125, and 150 original sampling points, respectively, illustrating the impact of spatial averaging on XCO_2 distribution. The base map was designed and developed by Esri | Powered by Esri.

https://doi.org/10.5194/egusphere-2026-3007
Preprint. Discussion started: 29 June 2026

Table 2. Information on the selected power plants.

Country	Name	Longitude	Latitude	UTC Time	Day or Night	Surface
South Africa	Majuba	29.77	-27.1	2024/6/1 13:41	Day	sand
South Africa	Majuba	29.77	-27.1	2024/6/8 13:43	Day	sand
India	Shree Singaji	76.53	22.1	2024/11/26 13:37	Day	forest
India	Lalitpur	78.65	24.796	2024/10/21 1:52	Night	forest
Russia	Surgut GRES-1 and 2	73.49	61.28	2024/8/28 2:26	Night	forest
China	Wucaiwan	89.11	44.69	2024/10/1 19:59	Night	sand
Russia	Reftinskaya GRES	61.71	57.11	2024/10/18 22:00	Night	forest

Table 3. Emission retrieval results for seven power plants under selected spatial averaging scales, compared with inventory datasets (Climate TRACE and Carbon Brief).

Name	Climate TRACE (kg s^{-1})	Carbon Brief (kg s^{-1})	Model result (kg s^{-1})	Averaging points	Wind speed (m s^{-1})	Wind direction (°)	Distance (km)
Majuba 6-1	691.83	644.97	806.70 ± 116.48	125	6.38	126.2	21.6
Majuba 6-8	691.83	644.97	850.97 ± 116.95	125	4.48	274.1	33.5
Shree Singaji	502.91	331.04	655.03 ± 82.68	150	3.34	236.9	45.6
Lalitpur	-	451.49	447.97 ± 103.04	75	4.96	98.6	48.1
Surgut GRES-1 and 2	987.53	-	1022.17 ± 144.46	150	4.68	355.7	27.2
Wucaiwan	614.17	645.28	583.67 ± 73.17	110	1.94	104.76	12.3
Reftinskaya GRES	806.45	626.93	884.07 ± 65.47	150	2.32	282.7	16.5

https://doi.org/10.5194/egusphere-2026-3007
Preprint. Discussion started: 29 June 2026

4 Conclusions and discussion

This study provides a systematic evaluation of the trade-off between spatial resolution and measurement precision in CO_2 point-source emission quantification using the DQ-1 spaceborne lidar. By integrating Allan deviation analysis with Gaussian plume simulations and selected real power-plant overpasses, we establish a quantitative framework for evaluating spatial averaging strategies. Our findings show that XCO_2 random errors over homogeneous surfaces decrease with increasing averaging length, from approximately 9.92 ppm at short averaging scales to about 1.06 ppm when averaged over 150 points (approximately 10.5 km). This scale-dependent error characterization reveals a nonlinear response of emission retrieval to spatial averaging: moderate averaging suppresses random noise and improves retrieval stability, whereas excessive averaging smooths the plume and can offset the benefit of noise reduction. Emission strength, transport distance, wind conditions, and local plume geometry jointly determine the preferred averaging scale. For strong idealized sources (2000 kg s^{-1}), moderate averaging provides the most stable retrievals in favorable cases, with R^2 values up to 0.68; however, the relative error increases substantially under larger transport distances or less favorable wind configurations. Weak sources (500 kg s^{-1}) remain close to the single-overpass detection limit even under optimized configurations. Applications to seven DQ-1 power-plant overpasses support the simulated scale dependence and show relatively good inventory consistency in several cases between 75 and 150 averaging points. This range should not be interpreted as a universal optimum. The comparisons are limited by the use of annual or multi-temporal inventories as references, the absence of globally available hourly plant operation data, and uncertainties in wind speed, plume height, atmospheric stability, background heterogeneity, and the Gaussian plume assumption. The results therefore should be interpreted as a retrieval-sensitivity and scale-optimization assessment rather than a complete validation of instantaneous power-plant emissions. A further nuance concerns the influence of background heterogeneity on the averaging process: when the background XCO_2 field on either side of the point source is imbalanced or contaminated by nearby sources, spatial averaging can shift the apparent XCO_2 maximum, bias the estimated plume center, and degrade retrieval accuracy. This effect is particularly important under nocturnal stable boundary layers or in regions with complex source distributions, where a linear background assumption may be insufficient. Future work should focus on multi-overpass aggregation, independent in situ or operational validation datasets, multi-source meteorological constraints, adaptive background fitting, and higher-resolution three-dimensional transport modeling to reduce uncertainties associated with instantaneous wind fields, background gradients, and plume dynamics.

Data availability

ERA5 data are available at https://cds.climate.copernicus.eu/#!/home. Carbon Brief data are available at https://www.carbonbrief.org/mapped-worlds-coal-power-plants/ (Carbon Brief, 2024). Climate TRACE data are available at https://climatetrace.org/explore/electricity-generation-co2e100-2024/ (Climate TRACE, 2023). The DQ-1/ACDL XCO_2 data used in this study were not publicly available at the time of submission because access is currently restricted to the mission

https://doi.org/10.5194/egusphere-2026-3007
Preprint. Discussion started: 29 June 2026

science team. The data can be requested from the corresponding author, subject to mission data-use approval. To support reproducibility, the case list, selected overpass metadata, averaging-scale settings, and derived retrieval results used in the analysis should be provided in the Supplement.

Supplement link

The link to the supplement will be included by Copernicus, if applicable.

Author contributions

RZ, LZ and XZ designed and directed the study. RZ, and LZ contributed to data analysis and wrote the first draft of this paper. MZ, XC, CC, and HY collected data. XZ, and PZ contributed to the data interpretation and review of the paper.

Competing interests

The contact author has declared that none of the authors has any competing interests.

Disclaimer

Publisher's note: Copernicus Publications remains neutral with regard to jurisdictional claims made in the text, published maps, institutional affiliations, or any other geographical representation in this paper. While Copernicus Publications makes every effort to include appropriate place names, the final responsibility lies with the authors.

Acknowledgements

We acknowledge the Shanghai Institute of Optics and Fine Mechanics, Chinese Academy of Sciences, and the National Satellite Meteorological Center for providing the DQ-1 data. We thank the teams that produce and maintain the ERA5, Climate TRACE, and Carbon Brief datasets used in this study. The satellite basemaps in Fig. 1 and Fig. 13 were obtained from Esri World Imagery. The authors used AI-based language polishing during manuscript preparation. All suggestions were reviewed and edited by the authors, who take full responsibility for the content of the paper.

Financial support

This research has been supported by the Jing-Jin-Ji Regional Integrated Environmental Improvement-National Science and Technology Major Project of Ministry of Ecology and Environment of China (No. 【2025ZD1200900】).

https://doi.org/10.5194/egusphere-2026-3007
Preprint. Discussion started: 29 June 2026

Review statement

The review statement will be added by Copernicus Publications listing the handling editor as well as all contributing referees according to their status anonymous or identified.

References

Piao, S., Fang, J., Ciais, P., Peylin, P., Huang, Y., Sitch, S., Wang, T., 2009. The carbon balance of terrestrial ecosystems in China. Nature 458, 1009–1013.

Arias, P., Bellouin, N., Coppola, E., Jones, R., Krinner, G., Marotzke, J., Naik, V., Palmer, M., Plattner, G.-K., and Rogelj, J.: Climate Change 2021: the physical science basis. Contribution of Working Group I to the Sixth Assessment Report of the Intergovernmental Panel on Climate Change; technical summary, 2021.

Friedlingstein, P., O'Sullivan, M., Jones, M.W., Andrew, R.M., Gregor, L., Hauck, J., Le Qu´er´e, C., Luijkx, I.T., Olsen, A., Peters, G.P., Peters, W., Pongratz, J., Schwingshackl, C., Sitch, S., Canadell, J.G., Ciais, P., Jackson, R.B., Alin, S.R., Alkama, R., Arneth, A., Arora, V.K., Bates, N.R., Becker, M., Bellouin, N., Bittig, H.C., Bopp, L., Chevallier, F., Chini, L.P., Cronin, M., Evans, W., Falk, S., Feely, R.A., Gasser, T., Gehlen, M., Gkritzalis, T., Gloege, L., Grassi, G., Gruber, N., Gürses, O., ¨Harris, I., Hefner, M., Houghton, R.A., Hurtt, G.C., Iida, Y., Ilyina, T., Jain, A.K., Jersild, A., Kadono, K., Kato, E., Kennedy, D., Klein Goldewijk, K., Knauer, J., Korsbakken, J.I., Landschützer, P., Lef˙evre, N., Lindsay, K., Liu, J., Liu, Z., Marland, G., Mayot, N., McGrath, M.J., Metzl, N., Monacci, N.M., Munro, D.R., Nakaoka, S.I., Niwa, Y., O'Brien, K., Ono, T., Palmer, P.I., Pan, N., Pierrot, D., Pocock, K., Poulter, B., Resplandy, L., Robertson, E., Rodenbeck, ¨ C., Rodriguez, C., Rosan, T.M., Schwinger, J., S´ef´erian, R., Shutler, J.D., Skjelvan, I., Steinhoff, T., Sun, Q., Sutton, A.J., Sweeney, C., Takao, S., Tanhua, T., Tans, P.P., Tian, X., Tian, H., Tilbrook, B., Tsujino, H., Tubiello, F., van der Werf, G.R., Walker, A.P., Wanninkhof, R., Whitehead, C., Willstrand Wranne, A., Wright, R., Yuan, W., Yue, C., Yue, X., Zaehle, S., Zeng, J., Zheng, B., 2022. Global carbon budget 2022. Earth Syst. Sci. Data 14, 4811–4900.

Andrew, R.M., 2020. A comparison of estimates of global carbon dioxide emissions from fossil carbon sources. Earth Syst. Sci. Data 12 (2), 1437–1465.

Cusworth, D.H., et al., 2021. Quantifying global power plant carbon dioxide emissions with imaging spectroscopy. AGU Adv. 2 (2) e2020AV000350.

Shi, T., Han, G., Ma, X., Mao, H., Chen, C., Han, Z., Pei, Z., Zhang, H., Li, S., Gong, W., 2023a. Quantifying factory-scale CO_2/CH4 emission based on mobile measurements and EMISSION-PARTITION model: cases in China. Environ. Res. Lett. 18, 034028.

Yang, S., Yang, J., Shi, S., Song, S., Luo, Y., Du, L., 2023. The rising impact of urbanization-caused CO_2 emissions on terrestrial vegetation. Ecol. Indic. 148, 110079.

Qin, X., et al., 2022. Global and regional drivers of power plant CO_2 emissions over the last three decades revealed from unit-based database. Earths Future 10 (10) e2022E F002657.

https://doi.org/10.5194/egusphere-2026-3007
Preprint. Discussion started: 29 June 2026

Schwandner, F.M., et al., Oct 2017. Spaceborne detection of localized carbon dioxide sources. Science 358 (6360), 192-+.

Dennison, P.E., et al., 2013. High spatial resolution mapping of elevated atmospheric carbon dioxide using airborne imaging spectroscopy: radiative transfer modeling and power plant plume detection. Remote Sens. Environ. 139, 116–129.

Shi, T., Han, G., Ma, X., Zhang, M., Pei, Z., Xu, H., Qiu, R., Zhang, H., Gong, W., 2020. An inversion method for estimating strong point carbon dioxide emissions using a differential absorption Lidar. J. Clean. Prod. 271, 122434.

Erland, B.M., Thorpe, A.K., Gamon, J.A., Dec 2022. Recent advances toward transparent methane emissions monitoring: a review. Environ. Sci. Technol. 56 (23),16567–16581.

Nassar, R., Hill, T.G., McLinden, C.A., Wunch, D., Jones, D.B.A., Crisp, D., 2017. Quantifying CO_2 emissions from individual power plants from space. Geophys. Res. Lett. 44, 10,045–10,053.

Zheng, T., Nassar, R., Baxter, M., 2019. Estimating power plant CO_2 emission using OCO-2 XCO_2 and high resolution WRF-Chem simulations. Environ. Res. Lett. 14 (8),085001.

Zheng, B., et al., 2020. Observing carbon dioxide emissions over China's cities and industrial areas with the orbiting carbon observatory-2. Atmos. Chem. Phys. 20 (14),8501–8510,2020.

Chevallier, F., et al., 2020. Local anomalies in the column-averaged dry air mole fractions of carbon dioxide across the globe during the first months of the coronavirus recession. Geophys. Res. Lett. 47 (22) e2020GL090244.

Nassar, R., Mastrogiacomo, J.-P., Bateman-Hemphill, W., McCracken, C., MacDonald, C. G., Hill, T., O'Dell, C.W., Kiel, M., Crisp, D., 2021. Advances in quantifying power plant CO_2 emissions with OCO-2. Remote Sens. Environ. 264, 112579.

Lin, X., et al., 2023. Monitoring and quantifying CO_2 emissions of isolated power plants from space. Atmos. Chem. Phys. 23 (11), 6599–6611.

Guo, W., Shi, Y., Liu, Y., and Su, M.: CO_2 emissions retrieval from coal-fired power plants based on OCO-2/3 satellite observations and a Gaussian plume model, Journal of Cleaner Production, 397, 136525, 2023.

Kiemle, C., Ehret, G., Amediek, A., Fix, A., Quatrevalet, M., Wirth, M., 2017. Potential of spaceborne lidar measurements of carbon dioxide and methane emissions from strong point sources. Remote Sens. 9, 1137.

Wang, N., Zhang, K., Shen, X., Wang, Y., Li, J., Li, C., Mao, J., Malinka, A., Zhao, C., Russell, L.M., Guo, J., Gross, S., Liu, C., Yang, J., Chen, F., Wu, L., Chen, S., Ke, J., Xiao, D., Zhou, Y., Fang, J., Liu, D., 2022b. Dual-field-of-view high-spectral-resolution lidar: simultaneous profiling of aerosol and water cloud to study aerosol–cloud interaction. Proc. Natl. Acad. Sci. 119, e2110756119.

Mao, J., Abshire, J.B., Kawa, S.R., Riris, H., Sun, X., Andela, N., Kolbeck, P.T., 2021. Measuring atmospheric CO_2 enhancements from the 2017 British Columbia wildfires using a lidar. Geophys. Res. Lett. 48, e2021GL093805.

Shi, T., Han, G., Ma, X., Pei, Z., Chen, W., Liu, J., Zhang, X., Li, S., and Gong, W.: Quantifying strong point sources emissions of CO_2 using spaceborne LiDAR: Method development and potential analysis, Energy Conversion and Management, 292, 117346, 2023

https://doi.org/10.5194/egusphere-2026-3007
Preprint. Discussion started: 29 June 2026

Ke, J., Sun, Y., Dong, C., Zhang, X., Wang, Z., Lyu, L., Zhu, W., Ansmann, A., Su, L., Bu, L., Xiao, D., Wang, S., Chen, S., Liu, J., Chen, W., Liu, D., 2022. Development of China's first space-borne aerosol-cloud high-spectral-resolution lidar: retrieval algorithm and airborne demonstration. PhotoniX 3, 17.

Fan, C., Chen, C., Liu, J., Xie, Y., Li, K., Zhu, X., Zhang, L., Cao, X., Han, G., Huang, Y., Gu, Q., Chen, W., 2024. Preliminary analysis of global column-averaged CO_2 concentration data from the spaceborne aerosol and carbon dioxide detection lidar onboard AEMS. Opt. Express 32, 21870–21886.

Zhang, X., Yang, H., Bu, L., Fan, Z., Xiao, W., Chen, B., Zhang, L., Liu, S., Wang, Z., Liu, J., Chen, W., Lee, X., 2024. Estimation of diurnal emissions of CO_2 from thermal power plants using spaceborne IPDA lidar. EGUsphere 2024, 1–22.

Han, G., Huang, Y., Shi, T., Zhang, H., Li, S., Zhang, H., Chen, W., Liu, J., Gong, W., 2024. Quantifying CO_2 emissions of power plants with aerosols and carbon dioxide Lidar onboard DQ-1. Remote Sens. Environ. 313, 114368.

Kruse, F. The Effects of Spatial Resolution, Spectral Resolution, and SNR on Geologic. In Proceedings of the 9th JPL Airborne Earth Science Workshop, Monterey, CA, USA, 27 February–2 March 2001.

Brunner, D., et al., 2023. Evaluation of simulated CO_2 power plant plumes from six high-resolution atmospheric transport models. Atmos. Chem. Phys. 23 (4), 2699–2728.

Jiang, Y.; Zhang, L.; Zhang,X.; Cao, X.; Dou, H.; Zhang, L.; Yan, H.; Wang, Y.; Si, Y.; Chen, B. Instrument Performance Analysis for Methane Point Source Retrieval and Estimation Using Remote Sensing Technique. Remote Sens. 2025, 17, 634. https://doi.org/10.3390/rs17040634.

Wu, Y., X. Chen, J. Liu, D. Chen, L. Zhou, X. Bao, Y. Song, and W. Chen, 2024: Silicon photonics integrated dual-wavelength frequency stabilized laser for spaceborne CO_2 gas measurement LiDAR. Opt. Express, 32, 46958, https://doi.org/10.1364/OE.537401.

C. TRACE, 2023. Greenhouse Gas Emissions Data-Climate TRACE.

Hersbach, H., et al., 2020. The ERA5 global reanalysis. Q. J. R. Meteorol. Soc. 146 (730),1999–2049.

Hu, Y. and Shi, Y.: Estimating CO_2 emissions from large scale coal-fired power plants using OCO-2 observations and emission inventories, Atmosphere, 12, 811, 2021.

Gelaro, R., McCarty, W., Suárez, M. J., Todling, R., Molod, A., Takacs, L., Randles, C. A., Darmenov, A., Bosilovich, M. G., and Reichle, R.: The modern-era retrospective analysis for research and applications, version 2 (MERRA-2), Journal of climate, 30, 5419-5454, 2017.

Brusca, S., Famoso, F., Lanzafame, R., Mauro, S., Garrano, A. M. C., and Monforte, P.: Theoretical and experimental study of Gaussian Plume model in small scale system, Energy Procedia, 101, 58-65, 2016.

Bovensmann, H., Buchwitz, M., Burrows, J., Reuter, M., Krings, T., Gerilowski, K., Schneising, O., Heymann, J., Tretner, A., and Erzinger, J.: A remote sensing technique for global monitoring of power plant CO 2 emissions from space and related applications, Atmospheric Measurement Techniques, 3, 781-811, 2010.

https://doi.org/10.5194/egusphere-2026-3007
Preprint. Discussion started: 29 June 2026

Pasquill, F.: The estimation of the dispersion of windborne material. Meteor. Mag., 90, 33-49., 1976: Atmospheric dispersion parameters in Gaussian plume modeling, Part 11. Possible requirements for change in the Turner workbook values. EPA Publication No, EPA-600/4-76-030b, Environmental Protection Agency, Research Triangle Park …, 1961.

Beals, G. A.: Guide to local diffusion of air pollutants, Air Weather Service (MAC), US Air Force, 1971.

Reuter, M., Buchwitz, M., Schneising, O., Krautwurst, S., O'Dell, C. W., Richter, A., Bovensmann, H., and Burrows, J. P.: Towards monitoring localized CO_2 emissions from space: co-located regional CO_2 and NO2 enhancements observed by the OCO-2 and S5P satellites, Atmospheric Chemistry and Physics, 19, 9371-9383, 2019.

Tellier, Y., Pierangelo, C., Gibert, F., and Wirth, M.: Averaging bias correction for the future space-borne methane IPDA lidar mission MERLIN, Atmos. Meas. Tech., 11, 5865–5881, https://doi.org/10.5194/amt-11-5865-2018, 2018.